ACADEMIC PRESS

Available online at www.sciencedirect.com

SCIENCE DIRECT®

Journal of Computational Physics 186 (2003) 47–69

JOURNAL OF COMPUTATIONAL PHYSICS

www.elsevier.com/locate/jcp

A non-periodic 2D semi-Lagrangian Vlasov code for laser–plasma interaction on parallel computer

A. Ghizzo *, F. Huot, P. Bertrand

Laboratoire de Physique des Milieux Ionisés , UMR 7040 Université Henri Poincaré, BP 239 54506 Vandoeuvre les Nancy Cedex, France

Received 23 July 2001; received in revised form 26 September 2002; accepted 5 December 2002

Abstract

For the first time, a 2D electromagnetic and relativistic semi-Lagrangian Vlasov model for a multi-computer environment was developed to study the laser–plasma interaction in an open system. Numerical simulations are presented for situations relevant to the penetration of an ultra-intense laser pulse inside a moderately overdense plasma and the relativistic filamentation instability in the case of an underdense plasma. The Vlasov model revealed a rich variety of phenomena associated with the fast particle dynamics induced by the laser pulse as particle trapping, particle acceleration and relativistic self-induced transparency in overdense plasma. Attention was focused on the efficiency and stability properties on the numerical scheme and implementation facilities on massively parallel computers. Success of the semi-Lagrangian Vlasov model is enhanced by the good conservation of the continuity equation and stability of Maxwell system due to the fine description of the electron distribution function and particularly of the charge density and current density.

Keywords: Numerical methods; Plasmas

1. Introduction

The numerical integration of the Vlasov equation is one of the key challenges of computational plasma physics. Since the early days of this discipline, an intensive work on this subject has produced many different numerical schemes, which however, can be bunched together in two main groups. On the one hand, particle-in-cell (PIC) codes have proven to be useful in studying plasma dynamics even for 2D and 3D problems and complex geometries. However only a few particles per cell have been used particularly in 3D PIC codes leading to a high level of numerical noise, especially in regions of phase space where the density is low. These PIC codes, for situations relevant to laser–plasma interaction, may largely overestimate absorption of the laser light and therefore plasma heating because of intrinsic ''numerical heating''. On the

* Corresponding author.
E-mail address: Alain.Ghizzo@lpmi.uhp-nancy.fr (A. Ghizzo).

0021-9991/03/$ - see front matter
doi:10.1016/S0021-9991(03)00010-X

other hand Eulerian Vlasov codes or semi-Lagrangian Vlasov codes display an extremely low level of numerical noise and prove to be able to describe particle acceleration processes (see by instance [1,2], and for the 2D case [3]) or saturation of the relativistic modulational instability (RMI) in 2D periodic plasma (see by instance [4]). Unfortunately, these codes demand a stronger numerical effort than their particle counterparts and require the discretization of the whole phase space. For this reason little progress has been made on fast and accurate integration of the Vlasov equation in two and three dimensions for a magnetized plasma. But a knowledge of the non-linear evolution of the magnetized plasmas in two and three dimensions is indispensable in understanding the plasma physics of controlled thermonuclear fusion or physics of the laser–plasma interaction. Most of the problems in "open" plasma treated with Vlasov codes are 1D in space and based on the time splitting scheme introduced by Cheng and Knorr [5]. In this scheme, the Vlasov equation was integrated in the x–v phase space by splitting up the free streaming term and the acceleration term in such a way that the overall scheme is in second order in time step. However in the strongly relativistic regime of the laser–plasma interaction an unadapted use of the splitting scheme may lead to a bad density conservation and triggers numerical instability in the case of a 1D system (see by instance [6]). Recently a direct integration using a 2D full advection based on B-spline interpolation [6] was proposed for achieving accurate solution of the Vlasov–Maxwell system. In this paper we present results of 2D open semi-Lagrangian Vlasov (SLV) simulations of the ultra-intense electromagnetic pulse with a slightly overdense (or underdense) plasma and describe the new features of the 2D SLV code that made it possible for the first time to simulate, using a 2D causal Vlasov code, the penetration of a strong electromagnetic pulse in an overdense plasma by relativistic self-induced transparency, and the relativistic filamentation instability (RFI) in an underdense plasma. In this code, splitting scheme has been used and the integration of the Vlasov equation is made along their exact characteristics. The code exists in 1D1/2 and 2D geometries and runs on the Cray T3E (using 128 or 192 processors) and the vectorial NEC-SX5 computer at the IDRIS center (Orsay, France).

2. The 2D relativistic and electromagnetic Vlasov model

In this paper, we study the propagation of an ultra-intense linearly p-polarized laser light in a plasma along the x-direction with the use of a 2D relativistic SLV model. The electron distribution function $f(x,y,p_x,p_y,t)$ obeys the relativistic Vlasov equation

$$\frac{\partial f}{\partial t}+\frac{p_x}{m\gamma}\frac{\partial f}{\partial x}+\frac{p_y}{m\gamma}\frac{\partial f}{\partial y}+e\left(E_x+\frac{p_yB_z}{m\gamma}\right)\frac{\partial f}{\partial p_x}+e\left(E_y-\frac{p_xB_z}{m\gamma}\right)\frac{\partial f}{\partial p_y}=0, \tag{1}$$

where the Lorentz factor was given by

$$\gamma^2=1+\frac{p_x^2}{m^2c^2}+\frac{p_y^2}{m^2c^2}. \tag{2}$$

The electromagnetic field components (E_x,E_y,B_z) obey Maxwell equations:

$$\frac{\partial \mathbf{E}}{\partial t}-c^2\,\mathrm{rot}\,\mathbf{B}+\mathbf{J}/\varepsilon_0=0, \tag{3}$$

$$\frac{\partial \mathbf{B}}{\partial t}+\mathrm{rot}\,\mathbf{E}=0, \tag{4}$$

$$\mathrm{div}\,\mathbf{E}=\rho/\varepsilon_0, \tag{5}$$

$$\operatorname{div}\mathbf{B} = 0, \tag{6}$$

where the electron current density $\mathbf{J}$ and the charge density ρ (n_i being the ion density) are given by

$$\mathbf{J} = \int\int \frac{\mathbf{p}}{m\gamma} f \,\mathrm{d}p_x \,\mathrm{d}p_y \quad \text{and} \quad \rho = e\int\int f \,\mathrm{d}p_x \,\mathrm{d}p_y - en_i.$$

In our numerical experiments, we use normalized quantities: time t, space coordinates x, y and momentum coordinates p_x, p_y are, respectively, normalized to the inverse plasma frequency ω_{p}^{-1}, $c\omega_{\mathrm{p}}^{-1}$ and mc. The electric field components E_x, E_y and B_z are normalized to $m\omega_{\mathrm{p}}c/e$ and $m\omega_{\mathrm{p}}/e$. We adopt the periodic boundary conditions in the y-direction and the incident laser pulse is linearly polarized in the y-direction (p-polarization). The conditions for the left hand and right hand boundaries in the x-direction correspond the free propagation of the light without reflection.

3. The numerical parallel algorithm

The algorithm used here is similar to the one of Ref. [8] (corresponding to the integration of the Vlasov equation in a 2D periodic plasma along their characteristics) with improvements as described in [6], which now allow the full relativistic treatment using B-spline interpolation of the distribution function in the momentum space.

3.1. The time splitting problem

Let us first recall the principles of the semi-Lagrangian method (see [7,9]) for the Vlasov equation. We refer the reader to Sonnendrücker et al. for more details (see [6]). The Vlasov equation (1) can be written in the following form:

$$\frac{\partial f}{\partial t} + \mathbf{U}(\mathbf{X}, t) \cdot \nabla_X f = 0, \tag{7}$$

where $\mathbf{X}$ stands for the phase space coordinates (here $\mathbf{X} = (x, y, p_x, p_y)$) and $\mathbf{U}$ is a divergence-free vector field having up four components in the 2D case. Note that, since $\mathbf{U}$ is divergence-free, Eq. (7) can also be written in a conservative form

$$\frac{\partial f}{\partial t} + \operatorname{div}_X(\mathbf{U}(\mathbf{X}, t) f) = 0. \tag{8}$$

Splitting the components of $\mathbf{X}$ into two sets $\mathbf{X}_1$ and $\mathbf{X}_2$, Eq. (8) can then be written in the form

$$\frac{\partial f}{\partial t} + \operatorname{div}_{X_1}(\mathbf{U}_1(\mathbf{X}_1, \mathbf{X}_2, t) f) + \operatorname{div}_{X_2}(\mathbf{U}_2(\mathbf{X}_1, \mathbf{X}_2, t) f) = 0. \tag{9}$$

Moreover, it is well known (see for instance [6]) that solving separately

$$\frac{\partial f}{\partial t} + \operatorname{div}_{X_1}(\mathbf{U}_1(\mathbf{X}_1, \mathbf{X}_2, t) f) = 0, \tag{10}$$

$$\frac{\partial f}{\partial t} + \operatorname{div}_{X_2}(\mathbf{U}_2(\mathbf{X}_1, \mathbf{X}_2, t) f) = 0, \tag{11}$$

keeps the second-order accuracy for the whole equation (9) by alternating the solves.

It is now important to point out that the semi-Lagrangian scheme does not solve Vlasov's equation in the conservative form, but in the advective form to make full use of the backward characteristic method. Therefore if (and only if)

$$\mathrm{div}_{X_1}\mathbf{U}_1(\mathbf{X}_1,\mathbf{X}_2,t)=0, \tag{12}$$

$$\mathrm{div}_{X_2}\mathbf{U}_2(\mathbf{X}_1,\mathbf{X}_2,t)=0, \tag{13}$$

we get

$$\frac{\partial f}{\partial t}+\mathbf{U}_1\cdot\nabla_{X_1}f=0, \tag{14}$$

$$\frac{\partial f}{\partial t}+\mathbf{U}_2\cdot\nabla_{X_2}f=0, \tag{15}$$

and keep the second-order accuracy for the whole equation (7) by alternating the solves. This is the basis of the time splitting scheme providing the conditions (12) and (13) are fulfilled. This is obviously the case for the 1D electrostatic Vlasov equation. On the contrary, if Eqs. (12) and (13) are not true then splitting Eq. (7) is equivalent to solve advective equations with a source term

$$\frac{\partial f}{\partial t}+\mathbf{U}_1\cdot\nabla_{X_1}f=-f\,\mathrm{div}_{X_1}(\mathbf{U}_1), \tag{16}$$

$$\frac{\partial f}{\partial t}+\mathbf{U}_2\cdot\nabla_{X_2}f=-f\,\mathrm{div}_{X_2}(\mathbf{U}_2). \tag{17}$$

Although from the divergence-free property of the full advection field $\mathbf{U}$, we have

$$\mathrm{div}_{X_1}(\mathbf{U}_1)=-\mathrm{div}_{X_2}(\mathbf{U}_2), \tag{18}$$

the source term in (16) or (17) do not cancel exactly since in a time splitting scheme (16) and (17) are not solved at the same time. Therefore a necessary condition for the time splitting to preserve the conservative character of the Vlasov equation is that the advection fields $\mathbf{U}_1$ and $\mathbf{U}_2$ are both divergence free. Furthermore the conservation of the continuity equation

$$\frac{\partial \rho}{\partial t}+\mathrm{div}\mathbf{J}=\mathbf{0} \tag{19}$$

is also verified provided that the conditions (12) and (13) are fulfilled. Let us consider the simplified equation which takes into account relativistic effects

$$\frac{\partial f}{\partial t}+\frac{ep_yB_z}{m\gamma}\frac{\partial f}{\partial p_x}-\frac{ep_xB_z}{m\gamma}\frac{\partial f}{\partial p_y}=0, \tag{20}$$

we see clearly that

$$\mathrm{div}_{p_x}\left(\frac{ep_yB_z}{m\gamma}\right)=-\frac{ep_xp_yB_z}{m^3c^2\gamma^3}=-\mathrm{div}_{p_y}\left(-\frac{ep_xB_z}{m\gamma}\right)\neq 0. \tag{21}$$

This condition (21) implies the use of a direct 2D advection for solving (20).

3.2. The semi-Lagrangian method

We can now introduce the characteristics of (7), which are the solutions of the dynamical system

$$\frac{\mathrm{d}\mathbf{X}}{\mathrm{d}t} = \mathbf{U}(\mathbf{X}(t), t). \tag{22}$$

Let us denote by $\mathbf{X}(t; \mathbf{x}, s)$ the solution at time t whose value is $\mathbf{x}$ at time s. Taking $\mathbf{X}(t)$ to be a solution of Eq. (22), we have

$$\frac{\mathrm{d}}{\mathrm{d}t}(f(\mathbf{X}(t), t)) = \frac{\partial f}{\partial t} + \frac{\mathrm{d}\mathbf{X}}{\mathrm{d}t} \cdot \nabla_X f = \frac{\partial f}{\partial t} + \mathbf{U}(\mathbf{X}(t), t) \cdot \nabla_X f = 0, \tag{23}$$

which means that f is constant along their characteristics. This can also be written as

$$f(\mathbf{X}(t; \mathbf{x}, s), t) = f(\mathbf{X}(s; \mathbf{x}, s), s) = f(\mathbf{x}, s) \tag{24}$$

for any times t, s and phase space coordinate $\mathbf{x}$. It is this property which will be used in the semi-Lagrangian method to solve a discrete problem, which is defined by introducing a finite set of mesh points $(\mathbf{x}_m)_{m=1,\ldots,N}$ which may or not may be equally spaced. Then, given the value of the distribution function f at the mesh points at any given time step, we obtain the new value at mesh point $\mathbf{x}_m$ using that

$$f(\mathbf{x}_m, t_n + \Delta t) = f(\mathbf{X}(t_n, \mathbf{x}_m, t_n + \Delta t), t_n). \tag{25}$$

For each mesh point $\mathbf{x}_m$, f is computed in two steps:

1. Find the starting point of the characteristic ending at $\mathbf{x}_m$, i.e., $\mathbf{X}(t_n, \mathbf{x}_m, t_n + \Delta t)$.
2. Compute $f(\mathbf{X}(t_n, \mathbf{x}_m, t_n + \Delta t), t_n)$ by interpolation, as f is known only at mesh points at time t_n.

3.3. The semi-Lagrangian method for the 2D relativistic Vlasov method

As we saw in the previous section, the equation can be split into four 1D advections, namely

$$\frac{\partial f}{\partial t} + \frac{p_x}{m\gamma}\frac{\partial f}{\partial x} = 0, \tag{26}$$

$$\frac{\partial f}{\partial t} + \frac{p_y}{m\gamma}\frac{\partial f}{\partial y} = 0, \tag{27}$$

$$\frac{\partial f}{\partial t} + eE_x\frac{\partial f}{\partial p_x} = 0, \tag{28}$$

$$\frac{\partial f}{\partial t} + eE_y\frac{\partial f}{\partial p_y} = 0, \tag{29}$$

and one 2D advection given by Eq. (20).

Note that in Eq. (20) the advection field is not independent of the $\mathbf{p}$ advection variable. However the characteristics of (20) can be determined exactly. Hence, taken separately, these steps may be exactly integrated along their exact characteristics and therefore a better numerical stability of the global scheme can be obtained. These characteristics of Eq. (20) are usually given by

$$\frac{\mathrm{d}p_x}{\mathrm{d}t} = \frac{ep_yB_z}{m\gamma}, \tag{30}$$

$$\frac{\mathrm{d}p_y}{\mathrm{d}t} = -\frac{ep_xB_z}{m\gamma}. \tag{31}$$

Multiplying Eq. (30) by p_x and Eq. (31) by p_y, we see clearly that the Lorentz factor γ remains constant along the motion. The exact solution of previous equations (30) and (31) can be written in the form

$$p_x^* = p_x \cos\omega\Delta t - p_y \sin\omega\Delta t, \tag{32}$$

$$p_y^* = p_x \sin\omega\Delta t + p_y \cos\omega\Delta t, \tag{33}$$

where $\omega = eB_z/m\gamma$. A formal solution of Eqs. (26)–(29) is then straightforward and the different steps of the code are:

$$f^*(x,y,p_x,p_y) = f^n\left(x - \frac{p_x}{m\gamma}\frac{\Delta t}{2}, y, p_x, p_y\right), \tag{34}$$

$$f^{**}(x,y,p_x,p_y) = f^*\left(x, y - \frac{p_y}{m\gamma}\frac{\Delta t}{2}, p_x, p_y\right), \tag{35}$$

$$f^{3*}(x,y,p_x,p_y) = f^{**}\left(x, y, p_x - eE_x\frac{\Delta t}{2}, p_y\right), \tag{36}$$

$$f^{4*}(x,y,p_x,p_y) = f^{3*}\left(x, y, p_x, p_y - eE_y\frac{\Delta t}{2}\right), \tag{37}$$

$$f^{5*}(x,y,p_x,p_y) = f^{4*}\left(x, y, p_x^*, p_y^*\right), \tag{38}$$

$$f^{6*}(x,y,p_x,p_y) = f^{5*}\left(x, y, p_x, p_y - eE_y\frac{\Delta t}{2}\right), \tag{39}$$

$$f^{7*}(x,y,p_x,p_y) = f^{6*}\left(x, y, p_x - eE_x\frac{\Delta t}{2}, p_y\right), \tag{40}$$

$$f^{8*}(x,y,p_x,p_y) = f^{7*}\left(x, y - \frac{p_y}{m\gamma}\frac{\Delta t}{2}, p_x, p_y\right), \tag{41}$$

$$f^{n+1}(x,y,p_x,p_y) = f^{8*}\left(x - \frac{p_x}{m\gamma}\frac{\Delta t}{2}, y, p_x, p_y\right), \tag{42}$$

where n and $n+1$ denote the initial and final times $t_n = n\Delta t$ and $t_{n+1} = (n+1)\Delta t$. In (38) the distribution function is calculated by a tensor product cubic B-spline interpolation, f being known only at mesh points.

Hence, since the advection field for each previous step (except the step given by (38)) does not depend on the variable to be advected, step 1, given the starting point of the characteristic, is then straightforward. In the relativistic Vlasov equation (1), we still have $\partial_j(p_j/m\gamma) = 0$ for $j = x$ or y, but no such property for the force term which now depends on the Lorentz factor given by (2). A straightforward computation shows that we still have

$$\mathrm{div}_{\mathrm{p}}\left(e\mathbf{E} + \frac{e\mathbf{p}}{m\gamma} \times \mathbf{B}\right) = 0.$$

Hence we could split the equation into one 2D advection for the momentum and two 1D advections for the treatment of the physical space.

Remark. Let us recall a few properties of our model that have been derived in previous investigations [6]:

1. For the free particle motion described by

$$\frac{\partial f}{\partial t} + \frac{\mathbf{p}}{m\gamma} \cdot \nabla_X f = 0$$

the CFL (Courant–Friedrichs–Levy) condition is naturally satisfied due to the relativity since $\|\mathbf{p}/m\gamma\| < c$. However the strong relativistic effects met in laser–plasma interaction at high intensities, generate strong fields leading, in the Eulerian scheme, to small time steps since $\|e\mathbf{E}/m\omega_{\mathrm{p}}c\| \gg 1$. In the semi-Lagrangian method, the time step is not restricted by the usual CFL condition, but by the deformational Courant number $\|\nabla \mathbf{U}\Delta t\| < 1$, which is often less restrictive.

2. The Vlasov equation coupled with the Poisson or Maxwell system often contains filamentation, which has been one of the reasons why Vlasov simulations have been poorly considered, compared to PIC simulations which are insensitive to this problem. This problem appears already on the treatment of the motion of free particles described by the equation for $f(x, v, t)$,

$$\frac{\partial f}{\partial t} + v\frac{\partial f}{\partial x} = 0. \tag{43}$$

A Fourier transform on x-axis gives

$$\frac{\partial f}{\partial t} - \mathrm{i}kvf(k, v, t) = 0, \tag{44}$$

leading to a solution in the usual form

$$f(k, v, t) = f(k, v, 0)\exp(\mathrm{i}kvt). \tag{45}$$

We see in (45) that, as a function of v, $f(k, v, t)$ oscillates at the frequency kt. When this frequency reaches the inverse of Δv (Δv being the size of the velocity sampling) we cannot follow the exact solution of f. Indeed, the distribution function $f(k, v, t)$ is constant along the characteristic curves, which become close, so that phase space regions where $f(x, v, t)$ has different values come close together and steep gradients are generated. At some time in the simulation, the phase space grid becomes too coarse to follow these thin filaments. Furthermore this mechanism is strongly amplified by relativistic effects since electron relativistic parametric instabilities have already this tendency to generate thin filaments in phase space. Relativistic effects add the coupling between the momentum variables (see Eq. (20)). Now in the treatment of $f(x, v, t)$ by Eulerian codes we may here to interpolate and this operation may lead to numerical instability. The code must avoid these instabilities and provides a smoothing of the details of the velocity space, hoping that these details will not influence the subsequent evolution of the plasma. As a result, finite-difference

numerical simulations of the Vlasov equation usually do not suffer from the numerical instabilities driven by the filamentation.

In the non-relativistic case, one of the most popular methods leading to a correct treatment of the 1D Vlasov equation was given by Cheng and Knorr [5] and the method is based on the time splitting scheme and cubic spline interpolation of the distribution function. The semi-Lagrangian model we proposed here is a generalization of the method of Knorr and Cheng and we can treat a relativistic Vlasov equation and this method is the mean to obtain a particle method without numerical noise but the price to paid is that this method is more expensive than a PIC method in term of memory and computational time.

Another scheme for the Vlasov equation is the flux balance method (FBM) [3], and more recently [16], the positive and flux conservative PFC method [15]. The basic idea of this method is to compute the average of the Vlasov equation solution in each cell of the phase space grid by a conservative method. In the PFC method, the starting point is the FBM method, and the authors have introduced a slope corrector to ensure the preservation of positivity and the maximum of f. Unlike classical eulerian algorithms such as finite difference or finite volume schemes, these methods are also not restricted by the CFL condition on the time step. The PFC method enforces the conservation of the global mass and controls numerical oscillations of f. However this method seems to be more dissipative but remains a possible candidate for solving the relativistic Vlasov equation.

3.4. Maxwell equations

Maxwell's equations (3) and (4) can be written in the following form for a p-polarized linearly electromagnetic pulse:

$$\frac{\partial E_x}{\partial t} = -\frac{J_x}{\varepsilon_0} + c^2 \frac{\partial B_z}{\partial y}, \tag{46}$$

$$\frac{\partial E_y}{\partial t} = -\frac{J_y}{\varepsilon_0} - c^2 \frac{\partial B_z}{\partial x}, \tag{47}$$

$$\frac{\partial B_z}{\partial t} = \frac{\partial E_x}{\partial y} - \frac{\partial E_y}{\partial x}. \tag{48}$$

Eqs. (46)–(48) are then solved using a well-known leapfrog scheme leading to the following set of equations:

$$E_{x\ i+\frac{1}{2},j}^{n+\frac{1}{2}} = E_{x\ i+\frac{1}{2},j}^{n-\frac{1}{2}} + \frac{c^2\Delta t}{\Delta y}\left[B_{z\ i+\frac{1}{2},j+\frac{1}{2}}^{n} - B_{z\ i+\frac{1}{2},j-\frac{1}{2}}^{n}\right] - \frac{\Delta t}{2\varepsilon_0}\left(J_{x\ i+1,j}^{n} + J_{x\ i,j}^{n}\right), \tag{49}$$

$$E_{y\ i,j+\frac{1}{2}}^{n+\frac{1}{2}} = E_{y\ i,j+\frac{1}{2}}^{n-\frac{1}{2}} - \frac{c^2\Delta t}{\Delta x}\left[B_{z\ i+\frac{1}{2},j+\frac{1}{2}}^{n} - B_{z\ i-\frac{1}{2},j+\frac{1}{2}}^{n}\right] - \frac{\Delta t}{2\varepsilon_0}\left(J_{y\ i,j+1}^{n} + J_{y\ i,j}^{n}\right), \tag{50}$$

$$B_{z\ i+\frac{1}{2},j+\frac{1}{2}}^{n+1} = B_{z\ i+\frac{1}{2},j+\frac{1}{2}}^{n} + \frac{\Delta t}{\Delta y}\left[E_{x\ i+\frac{1}{2},j+1}^{n+\frac{1}{2}} - E_{x\ i+\frac{1}{2},j}^{n+\frac{1}{2}}\right] - \frac{\Delta t}{\Delta x}\left[E_{y\ i+1,j+\frac{1}{2}}^{n+\frac{1}{2}} - E_{y\ i,j+\frac{1}{2}}^{n+\frac{1}{2}}\right]. \tag{51}$$

3.5. Rigorous charge conservation for local electromagnetic fields solvers

It is well known, that given initial electromagnetic field (E_0, B_0), Maxwell's equations (3)–(6) have a unique solution in a well-chosen functional space, and that it suffices to consider Eqs. (3)–(6) (divergence

terms) being automatically satisfied as a consequence from (3) and (4) provided they are satisfied by the initial conditions. The source terms in Maxwell equations **J** and ρ satisfy the continuity equation (19).

However, when Eq. (19) is not exactly satisfied, which is the case generally in PIC computations where **J** and ρ are computed approximately from particle data, the Maxwell system (3)–(6) is then overdetermined and one has to discard a part of the information contained in the given **J** and ρ in order to get the solution. The first obvious approach to this problem, we have indeed adapted in the SLV code, is to still disregard Eqs. (5) and (6) and compute the solution only from (3) and (4) which is a well-posed problem. It is well known that, in PIC codes, although the error committed at each time step is small, these errors accumulate and long time computations become erroneous due to the lack of charge separation. A second approach, which is used in most PIC simulations, consists in still calculating the electric and magnetic field **E** and **B** from the two rotational Eqs. (3) and (4), but perform at every time step or from time to time a so-called Poisson correction, which consists in discarding the irrotational part of **E** and replacing it by the solution of the Poisson equation. We refer the reader to publications [11] and [12] for more details.

Success of the SLV model is enhanced by the property of good conservation of the continuity Eq. (19), due to the fact that the current density **J** and charge density ρ were directly evaluated by using the electron distribution function, which, in an eulerian description is noiseless. One also checks in semi-Lagrangian simulations that $\operatorname{div}\mathbf{E} - \rho/\varepsilon_0$ remains small by virtue of the conservation condition (19) on the charge density. The resulting error in $\operatorname{div}\mathbf{E} = \rho/\varepsilon_0$ remains small during the simulation.

Let us now go through the steps of the algorithm for the electromagnetic model. Thanks to the Splitting method that we use, the semi-Lagrangian method can be applied once for the 2D physical space advection (or two 1D physical are also possible), with the velocity $\mathbf{v} = \mathbf{p}/m\gamma$ as a parameter, and once for a 2D momentum space advection; with the physical space coordinate **r** as a parameter. Thus, if the data are distributed in each case according to the parameter, there will be no communication at all. The computations in this case, which are fully local, involve multiple tridiagonal solves for the cubic spline interpolation, and explicit computations for the Spline evaluation. Details of the parallelization of the code can be found in [10].

3.6. The parallel algorithm

The Vlasov–Maxwell system is solved numerically using the time splitting scheme, which involved here five steps. Normally, for a 4D problems like ours, a global 3D or 4D decomposition is optimal, since it has the smallest interprocessor boundary and involves no data distribution on the processors. However tridiagonal solves (required for computing the cubic B-spline or cubic spline coefficients) are well known not to have very good scalability when performed on multiple processors. On the other hand, we saw that, for each stage of the algorithm, there is a 1D band (or 2D band) decomposition for which there is a natural optimal parallelism. Therefore our final choice was to take several distinct decompositions, even through this would involve global communication. One primary decomposition in 1D bands in the p_x-direction for the distribution function and 1D bands in the x-direction for f.

Step 1: Compute the electric field at time $t_{n+1/2}$ using Eqs. (49) and (50). The current density $\mathbf{J}^n$ was evaluated exactly at time $t_n = n\Delta t$ through the data of the electron distribution function using extended integration formula constructed by fitting cubic polynomials through successive groups of four points and with the same order as Simpson's rule (for more details see [13], pp. 128–129).

Step 2: Perform the shift over $\Delta t/2$ of the distribution function in the x- and y-directions using Eqs. (34) and (35).

Step 3: Compute the magnetic field $B_{z\ i+\frac{1}{2},j+\frac{1}{2}}^{n+1}$ using Eq. (51) and calculate the field $B_z^* = (B_z^n + B_z^{n+1})/2$ at time $t_{n+1/2}$.

Step 4: Transpose the distribution function in order to obtain a decomposition domain in the x-direction for f and shift the transposed function ${}^t f$ for a time step in the **p** space using the sequence of Eqs. from (36)–

(40) using the exact characteristics (32) and (33). Then we transpose again ${}^t f$ to obtain the 1D bands in the p_x-direction.

Step 5: Shift f for half a time step $\Delta t/2$ in the x and y-direction using again Eqs. (42) and (41). The error in the charge density conservation is then evaluated at each time step using

$$\varepsilon_{i,j}^{n+1} = \frac{\rho_{i,j}^{n+1} - \rho_{i,j}^{n}}{\Delta t} + \frac{J_{x\ i+1,j}^{n+\frac{1}{2}} - J_{x\ i-1,j}^{n+\frac{1}{2}}}{2\Delta x} + \frac{J_{y\ i,j+1}^{n+\frac{1}{2}} - J_{y\ i,j-1}^{n+\frac{1}{2}}}{2\Delta y}. \tag{52}$$

4. Numerical tests

In this section, we present a first series of numerical tests corresponding to the propagation of an ultra-intense linearly polarized laser beam in an overdense plasma along the x-direction. It is well known that a high frequency electromagnetic pulse, with frequency ω_0 less than the electron plasma frequency ω_p, cannot propagate in a plasma. But if the intensity of the pump wave is sufficiently intense, to make electrons relativistic, the cutoff frequency ω_p is then modified due to relativistic effects. Two penetration mechanisms have been considered: relativistic self-induced transparency and conventional hole boring or forward motion of the critical surface due to the ponderomotive pressure.

Here we focus on the propagation of high intensity pulse inside a slightly overdense plasma of density $n_e = 2n_{crit}$, where n_{crit} is the critical density. The plasma consists of electrons with initial temperature of

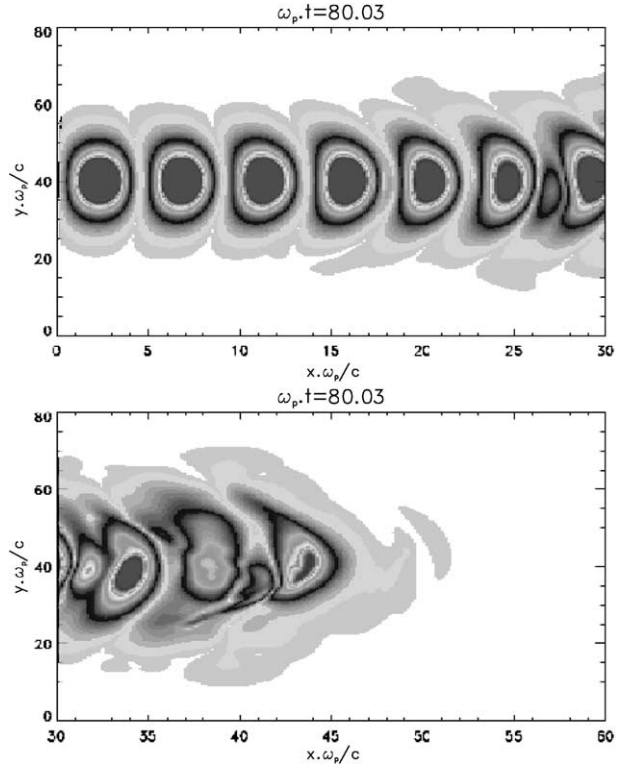

Fig. 1. Penetration of the Poynting vector inside the overdense plasma at time $t\omega_p = 80$ by relativistic self-induced transparency. The periodic structure of the electromagnetic pulse is clearly apparent.

$T_e = 5$ keV and fixed ions, forbidding the conventional hole boring process. The size of the simulation box is $L_x\omega_p/c = 60$ ($\sim 6.75\lambda_0$ where λ_0 is the laser wavelength) along x and $L_y\omega_p/c = 80$ ($\sim 9\lambda_0$) along y. We adopt the periodic boundary conditions in the y-direction. The incident p-linearly polarized wave has a gaussian transverse intensity profile with a peak intensity of $I\lambda_0^2 = 8.20 \times 10^{18}$ W μm^2 cm^{-2}. This intensity corresponds to $a_0 = p_{osc}/mc = \sqrt{6}$. The phase space sampling used here is $N_xN_yN_{p_x}N_{p_y} = 384 \times 128 \times 128 \times 64$, i.e., 402 10^6 grid points or "particles". Typical time step used in simulation are $\Delta t\omega_p = 0.025$ or 0.05.

Figs. 1 and 2 show, respectively, at time $t\omega_p = 80$ and $t\omega_p = 120$ the penetration of the Poynting vector inside the overdense plasma. Extremely intense quasi-static magnetic field corresponding to $100MG$ (not shown here) have been observed in the simulation to form in the overdense plasma. The periodic structure of the light is apparent in Fig. 1 while we see in Fig. 2 a more complex structure due to the incident and reflected parts of the electromagnetic wave. One of the basic effects shown in simulation is thus the possibility for a strong laser pulse to propagate in the overdense plasma by relativistic self-induced transparency. Indeed the optical properties of plasma are determined not by the electron rest mass but by its relativistic mass. As a consequence, for a sufficiently high amplitude of the laser beam inside the plasma, the quiver motion of plasma electrons can enlarge their relativistic mass. This mechanism is apparent in Fig. 3 which is a plot of the electron relative density $\eta = \int f/\gamma \, dp_x \, dp_y$ at time $t\omega_p = 80$. The corresponding curve at time $t\omega_p = 120$ is displayed in Fig. 4. The laser pulse penetrates inside the overdense plasma by relativistic self-induced transparency creating a channel in plasma density. As illustrated in Fig. 4, the depth of the hole increased with time. As the hole forms, the penetration of the laser light leads to a strong local absorption of the incident pump wave energy to plasma. This penetration of the laser pulse is associated with the plasma wave breaking giving rise to a strong plasma electron trapping mechanism.

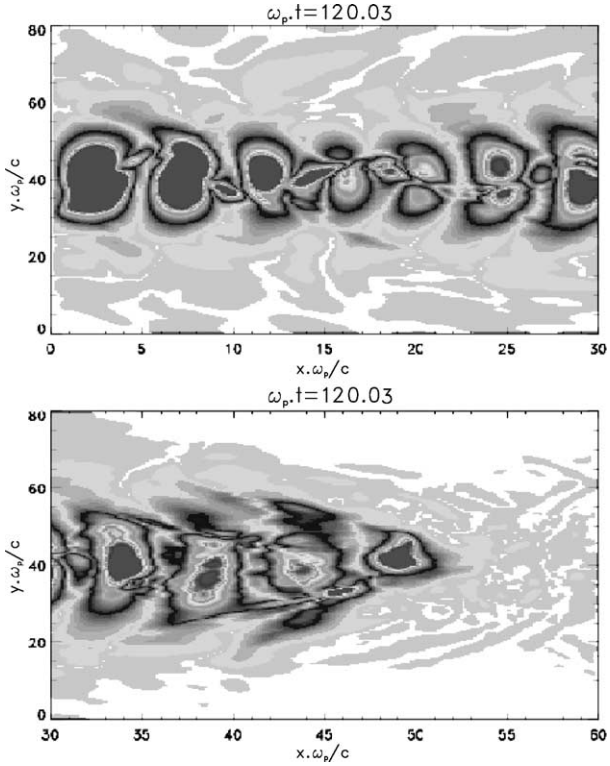

Fig. 2. Same representation as in Fig. 1 but at later time $t\omega_p = 120$ showing a more complex structure due to the incident and reflected parts of the electromagnetic pulse.

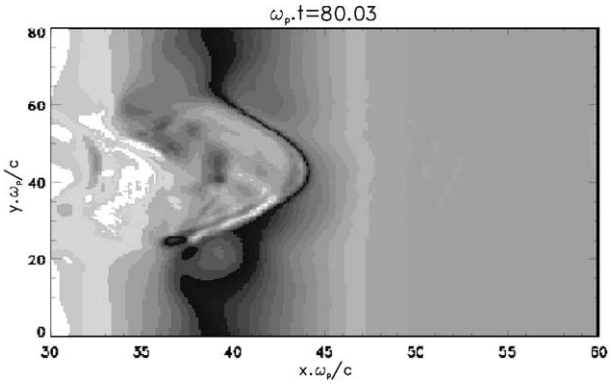

Fig. 3. The relative electron density computed at time $t\omega_p = 80$. We see clearly that the laser beam penetrates inside the overdense plasma by self-induced transparency creating a hole in the electron density.

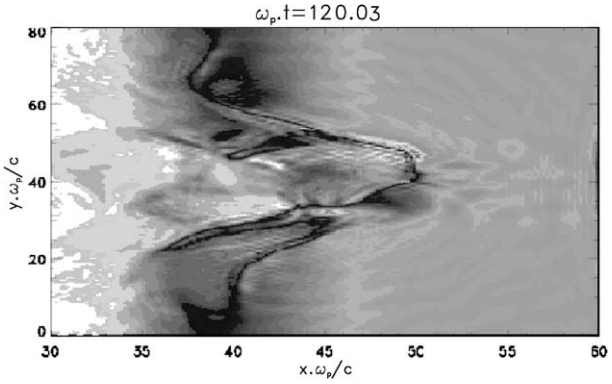

Fig. 4. The corresponding representation at time $t\omega_p = 120$. As illustrated in the figure, the depth of the hole increased with time.

The charge density ρ and the current density $\mathbf{J}$ are derived from the electron distribution function and satisfy the charge continuity equation. Note in this case if the charge conservation condition can be satisfied rigorously numerically, one can update the electromagnetic field using only the two curl Maxwell equations. Numerical experiments performed here have shown that the charge conservation condition is fulfilled satisfactorily. Finally we test the complete (field plus "particle") SLV code using charge conservation as a local measure of code accuracy. In Figs. 5 and 6 we have plotted $\delta\varepsilon = \partial\rho/\partial t + \operatorname{div}\mathbf{J}$ at two different times of plasma evolution $t\omega_p = 80$ and 120, as a measure of the numerical error generated by the field solve. We see clearly that $\delta\varepsilon$ remains small. Numerical tests, not shown here, indicate that the error is reduced significantly as one improves the phase space grid resolution. It is well known that the noise properties observed in electromagnetic PIC simulations were related to the methods of forming $\mathbf{J}$, not to the use of electromagnetic fields. Methods for calculating a charge conserving $\mathbf{J}$ have been discussed for ρ obtained by Nearest-Grid-Point weighting [14]. The latter authors found that the noise level in the electromagnetic fields rose in time at an inconveniently rapid rate. It is not the case here, when the current density is directly obtained through the data of the electron distribution function.

The most striking advantage, however, of the Vlasov code (already demonstrated in a 1D open-system (see by instance [1,2]) is the very fine resolution of the distribution function in phase space, capable of resolving the finest mechanisms of wave–particle interaction. We are able to evaluate accurately the current density $\mathbf{J}$ in the laser plasma interaction. Figs. 7 and 8 show the behavior of the current density obtained by

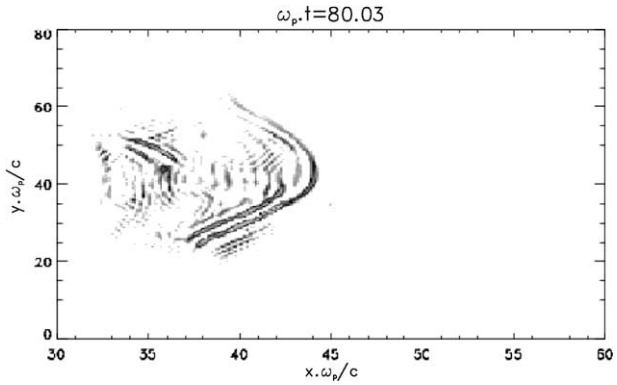

Fig. 5. Measure of the local charge conservation obtained by semi-Lagrangian Vlasov simulation at time $t\omega_p = 80$: numerical experiment performed here shows that the charge conservation ($\delta\varepsilon$) condition is fulfilled satisfactorily.

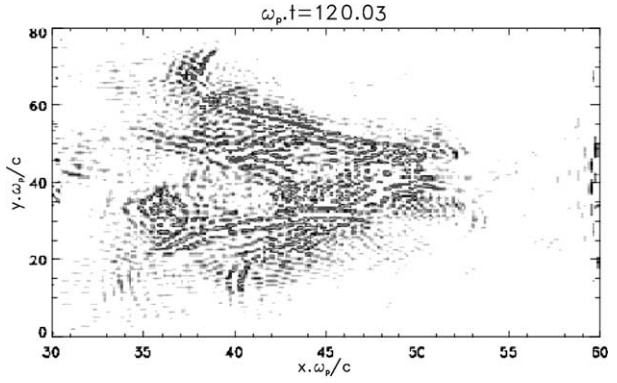

Fig. 6. Measure of local charge conservation at later time $t\omega_p = 120$. The current density has been directly obtained through the data of the electron distribution function, which in eulerian description is ''noiseless''.

the SVL model at time $t\omega_p = 80$ and 120. As shown in Fig. 7, the laser beam propagation inside the overdense plasma induced by relativistic self-induced transparency gives rise to a strong peak in the current density inside the overdense plasma located near the channel. Fig. 8 displays the complex structure of the current density later at $t\omega_p = 120$. As the pulse continues to propagate, the local absorption (described by the term $\mathbf{J} \cdot \mathbf{E}$) increases as the hole depth increases. The plasma current increases in intensity and the peaks are located on the wall of the channel, as can be seen in Fig. 8.

To benchmark the performance of this code, we present timing result from running this code on the Cray T3E parallel supercomputer and comparisons have been made with the NEC-SX5 vectorial supercomputer at the IDRIS center. The Cray T3E at IDRIS has 256 Alpha EV5 processors, each with peak speed of 600 Mflops, and the total memory size is 32 GB while the NEC-SX5 computer has 40 vectorial nodes, each of 8 Gflops. The vectorized version of the Vlasov code achieved a data processing rate of 1.9 Gflops (for one processor) and demonstrated a reasonably high vectorized efficiency. Different phase space grid $N_x N_y N_{p_x} N_{p_y} = 384 \times 128 \times 128 \times 64$ and $288 \times 96 \times 144 \times 96$ were investigated resulting in a corresponding number of 402 and 382 millions of particles. The total CPU time was close to 0.28 μs per time step per particle on the NEC-SX5 computer while the parallelized version of the Vlasov code gives 16.0 μs per time step per particle and per processor.

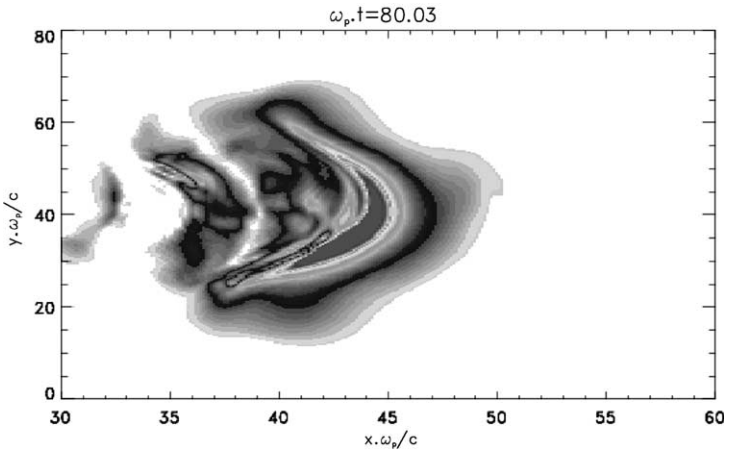

Fig. 7. Current density behavior in real space at time $t\omega_p = 80$, indicating the penetration mechanism of the intense laser pulse: we see clearly a strong peak in the current density located near the hole.

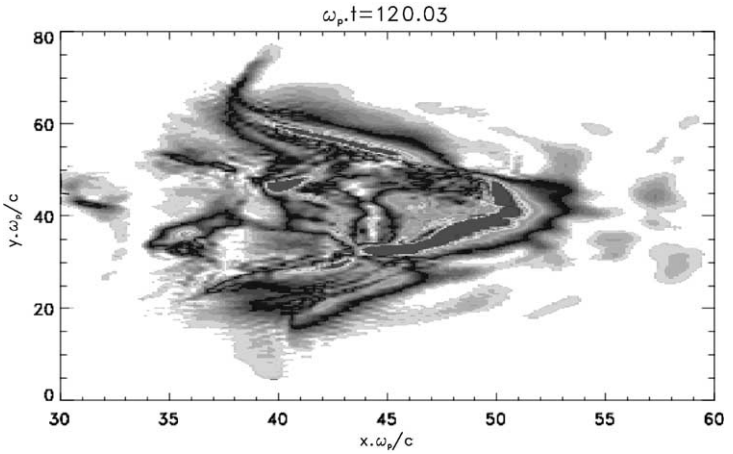

Fig. 8. Current density behavior at later time $t\omega_p = 120$ in time evolution showing now a more complex structure and high local absorption in plasma.

5. Filamentation aspect in phase space induced by relativistic parametric instabilities

In this section we present two examples with particular emphasis on particle dynamics and the filamentation phenomena in phase space. To demonstrate the efficiency of our algorithm and the high level of the complexity induced by Vlasov equation in cartesian geometry, a second series of numerical simulations has been carried out in order to analyze in detail the wave–particle dynamics met in the relativistic regime of the laser–plasma interaction in moderately overdense (and underdense) plasma. It is well known that electromagnetic waves are parametrically unstable when they propagate through a plasma. At low intensities ($a_0 \ll 1$), they are clearly identified as stimulated Raman scattering (SRS). Relativistic effects add the relativistic modulational instability (RMI) and the relativistic filamentation instability (RFI). There are two aspects of the same instability, the wave vector being, respectively, parallel and perpendicular to the wave

vector of the pump wave. Vlasov simulations provide an excellent description of small-scale phase space dynamics although the filamentation mechanism (or phase space mixing) is saturated by some numerical dissipation induced by the numerical scheme.

5.1. 1D SLV simulation of self-induced transparency in an overdense plasma

Although the demanding causal simulations are necessary to understanding realistic case, these simulations are also difficult to analyze in detail, sufficient to gain even qualitative physical understanding. One of the difficulties is that even the simplest cases of a plasma wave (with a given wave number) involve the growth of the harmonic modes, involving several plasma modes in the system loading to a more complicated structure in phase space. It is in particular the case of Fig. 9 obtained in the case of a 1D periodic plasma, showing the x–p_x phase space structures and in particular the occurring of a vortex structure in rotation with the formation of thin filaments. This simulation has been carried out using a 1D simplified model with Dirac distribution function in the $\mathbf{p}_\perp$ transverse direction $\delta(\mathbf{p}_\perp - \mathbf{P}_\perp(x,t))$ which corresponds to consider the plasma to be cold in the transverse direction, the electron distribution function depends in that case only to the x and p_x phase space coordinates. Details of the model are given in [17]. The initial homogeneous Maxwellian distribution function has a temperature of 3 keV. The initial large amplitude pump wave (ω_0, k_0) is taken as

$$\mathbf{E} = (0, E_0 \cos k_0 x, E_0 \sin k_0 x). \tag{53}$$

(ω_0, k_0) satisfy the relativistic dispersion relation of circularly polarized waves $\omega_0^2 = \omega_p^2/\gamma_0 + k_0^2 c^2$ with a Lorentz factor given by $\gamma_0^2 = 1 + a_0^2$. Choosing $k_0 c/\omega_p = 1/\sqrt{2} = 2\Delta k$ ($\Delta k = 2\pi/L$ being the fundamental wave number and L the length of the plasma box) and $a_0 = \sqrt{3}$ (which corresponds to an irradiation of $I = 8.2 \times 10^{18}$ W cm^{-2} for an electromagnetic wave length of 1 μm), we obtain $\omega_0 = \omega_p$ (i.e., a ratio of the electron plasma density to the critical density of $n_e/n_{crit} = 1$ or $n_e/\gamma_0 n_{crit} = 0.5$). We have used a phase space sampling of $N_x N_{p_x}$ of 512×768 points and a time step of $\Delta t \omega_p = 0.010$. Here the formation of smaller and smaller scales in phase space results from a physical process induced by the relativistic parametric instability. Such a phenomena occurs even in a simple geometry (Cartesian) using periodic boundary conditions and plays a major role in causal simulations. To reduce the influence of this microstructure, we have increase the electron temperature to $T_e = 12$ keV in 2D simulations. Although the previous model was simplified, it gives some insight in the behavior of the electron distribution in phase space.

We consider now a 1D1/2 simulation in the case of the interaction of a p-polarized electromagnetic wave of quiver momentum $a_0 = 2$ with an 1D plasma of density $n_e/n_{crit} = 1.60$. The laser pulse propagates in the x-direction and is normally incident on an inhomogeneous density profile. We have used a phase space sampling of $N_x N_{p_x} N_{p_y}$ of $769 \times 193 \times 129$ or 19 millions of grid points or "particles". The time step is $\Delta t \omega_p = 0.0375$. The initial electron plasma temperature is $T_e = 12$ keV in both p_x- and p_y-directions. Figs. 10 and 11 show, respectively, the x–p_x and x–p_y phase space representation. Although the behavior of the distribution function remains simple in the x–p_y phase space, the electron distribution function exhibits a strong modulation induced by the relativistic quiver velocity of particles. The behavior is more complex in the x–p_x phase space where we can see clearly the formation of filaments at time $t\omega_p = 135$, leading to a three-vortex structure at later time $t\omega_p = 202.5$ as the result of a phase space mixing. The induced transparency has been related to a Doppler shift of the electromagnetic wave reflected by the discontinuity associated with the wave front propagation. This discontinuity, located at $x\omega_p/c \simeq 80$ at $t\omega_p = 202.5$, acts as a mirror for the incoming laser light which is reflected with the Doppler shift. This reflected electromagnetic light of frequency ω_r and wave number k_r beats with the incoming pump wave of frequency ω_0 and wave number k_0 inside the plasma leading to the formation of a plasma wave of frequency $\omega_0 - \omega_r$ and wave number $k_0 + k_r$. As a result of this beat process, vortices

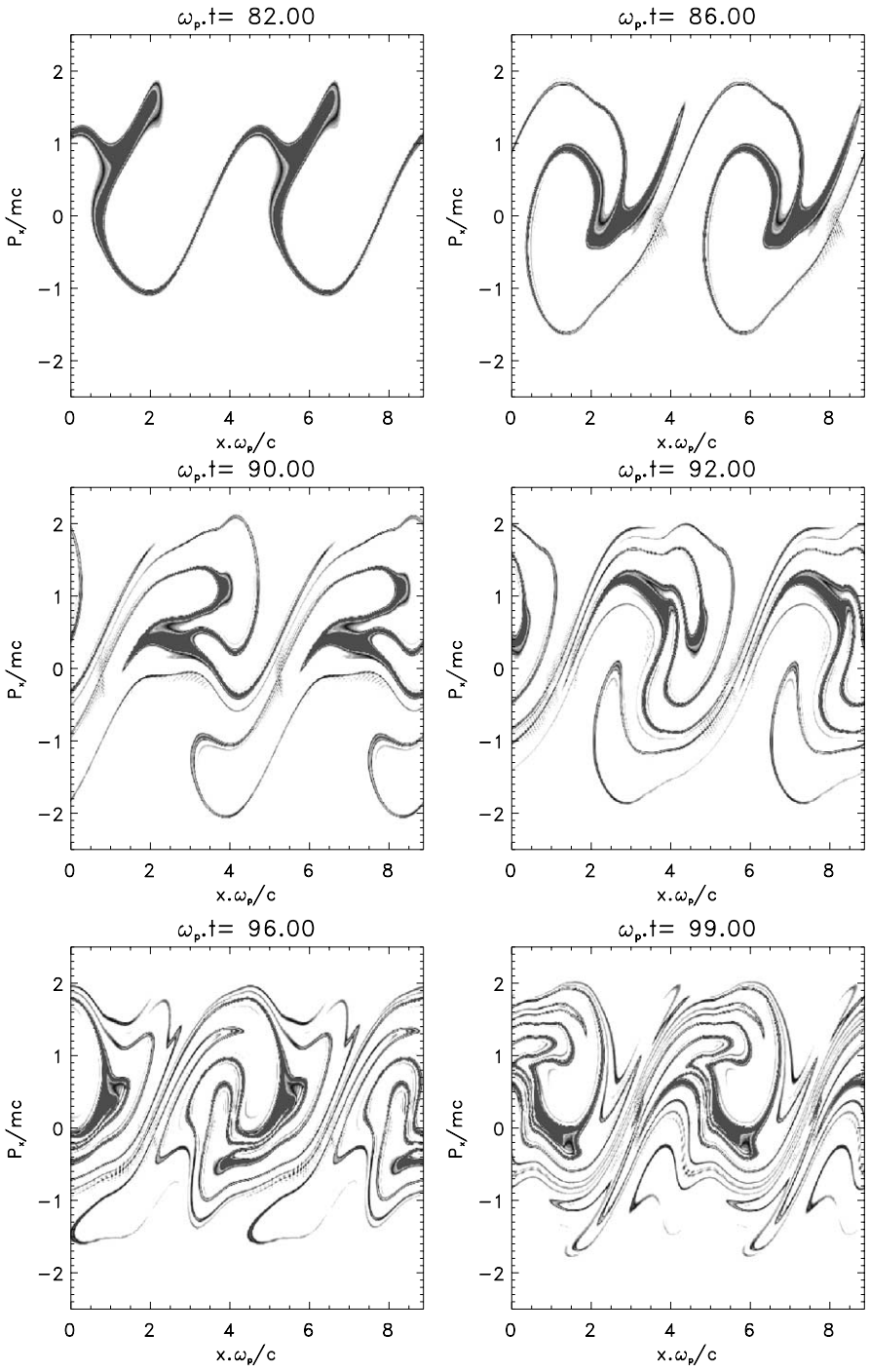

Fig. 9. x–p_x phase space representation of the distribution function obtained using 1D periodic simulation showing the formation of the microstructure. The parameters are $n/n_{\mathrm{crit}} = 1$ and $a_0 = \sqrt{3}$.

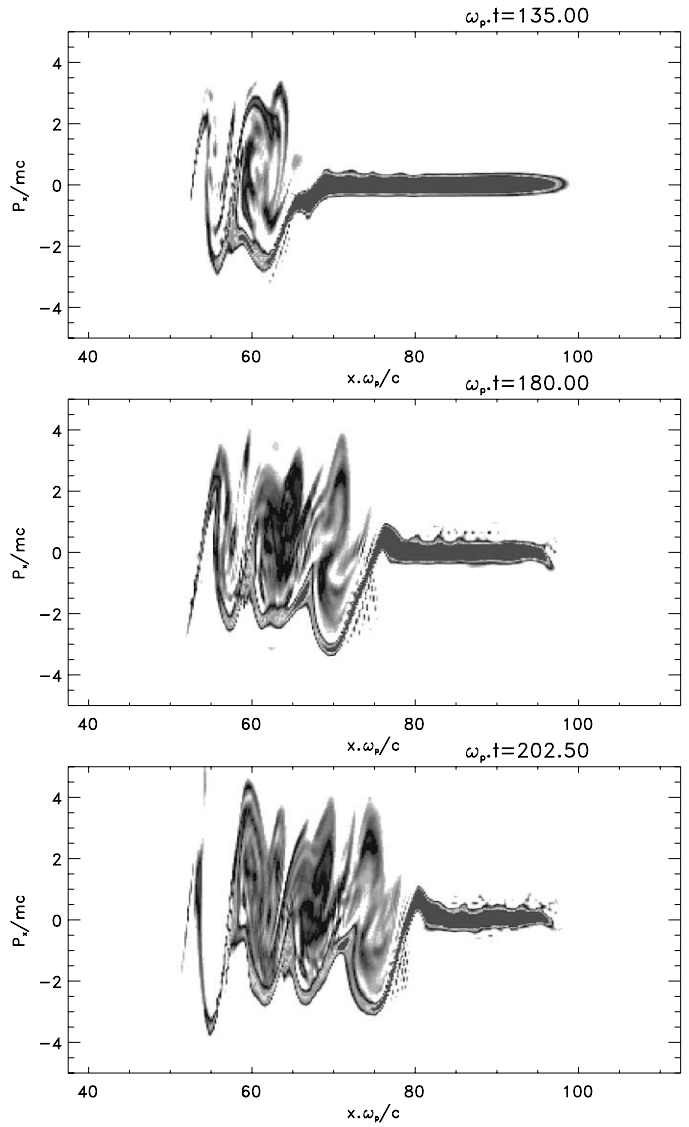

Fig. 10. x–p_x phase space representation obtained with causal simulation including the propagation of a linearly polarized wave with a normalized quiver momentum of $a_0 = 2$ inside an overdense plasma of density $n_e = 1.6 n_{crit}$ at three different times during the evolution.

are generated in the phase space. Very fine physical phenomena can then be successfully obtained in that case using a SLV code.

5.2. 2D causal simulation of RFI

We discuss now a specific example of 2D causal simulation of the evolution of the RFI which is initiated by the refraction of the laser light into regions of low relative plasma density. In that case spatial transverse effects are important and implies 2D simulations. The process of RFI itself leads to non-uniform illumination and to the self-focusing of a laser beam which may give rise to an amplification of the laser peak

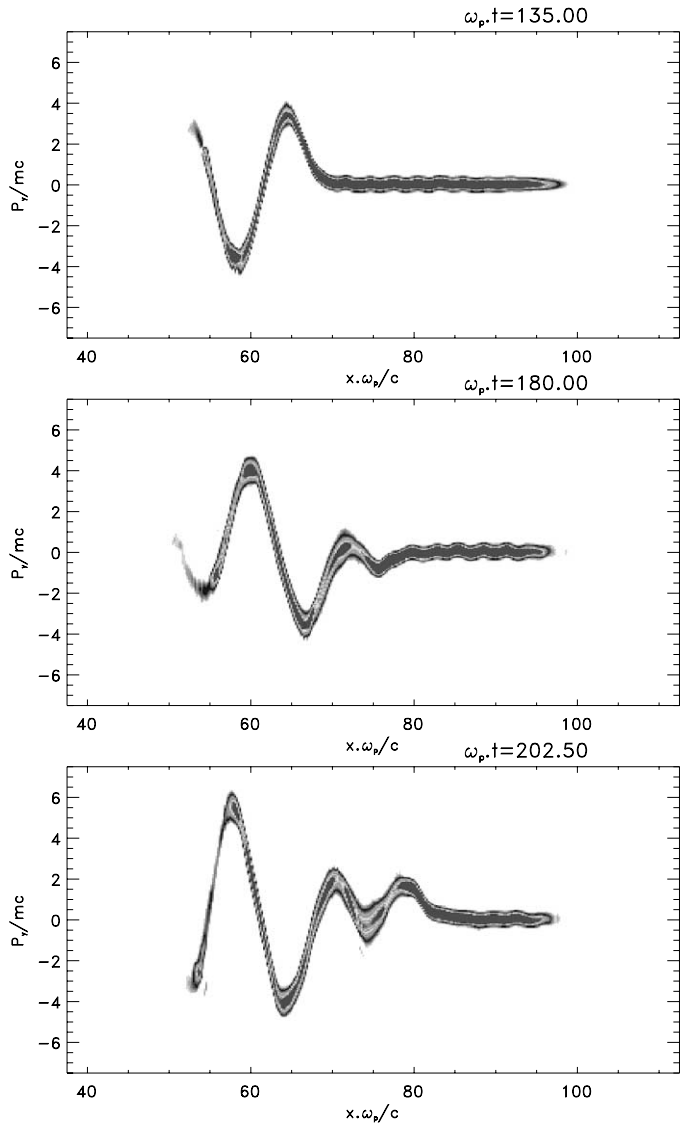

Fig. 11. Corresponding x–p_y phase space representation showing the strong modulation of the function induced by the relativistic quiver velocity of particles.

intensity so that the electron parametric instability as SRS or RMI will develop preferentially in those spatially localized regions of high intensity constituted by the filaments of the laser pulse. Thus RFI interacts with other kinetic processes, in particular parametric instabilities as SRS, which can grow fastest in filaments.

The physical parameters are $a_0 = \sqrt{3}$ and $n_e/n_{crit} = 0.50$ corresponding now to the growth of the RMI in an underdense plasma. We have used a phase space sampling of $N_x N_y N_{p_x} N_{p_y} = 768 \times 128 \times 192 \times 32$ or 603×10^6 grid points to describe the electron distribution function. The electromagnetic wave field $eE_y/m\omega_p c$ has an uniform transverse profile plus a small perturbation, its expression reads

$$\frac{eE_y}{m\omega_{\mathrm{p}}c}(x=0,y,t)=\frac{eE_0}{m\omega_{\mathrm{p}}c}\sin^2\left(\frac{\pi t}{2\tau}\right)\left(1+\sum_{i=1}^{6}\beta_i\sin(\mathrm{i}\Delta k_y y)\right)\sin(\omega_0 t), \tag{54}$$

where τ is the rise time of the electromagnetic pulse and $\Delta k_y = 2\pi/L_y$ the fundamental mode in the y-direction. We have used $\beta_i = 0.010$ for $i = 1,\ldots,6$. We have plotted in Fig. 12 the quantity

$$\mathbf{S}=\frac{\mathbf{E}\times\mathbf{B}}{\mu_0}+mc^2\int\int(\gamma-1)\frac{\mathbf{p}}{m\gamma}f\,\mathrm{d}p_x\,\mathrm{d}p_y, \tag{55}$$

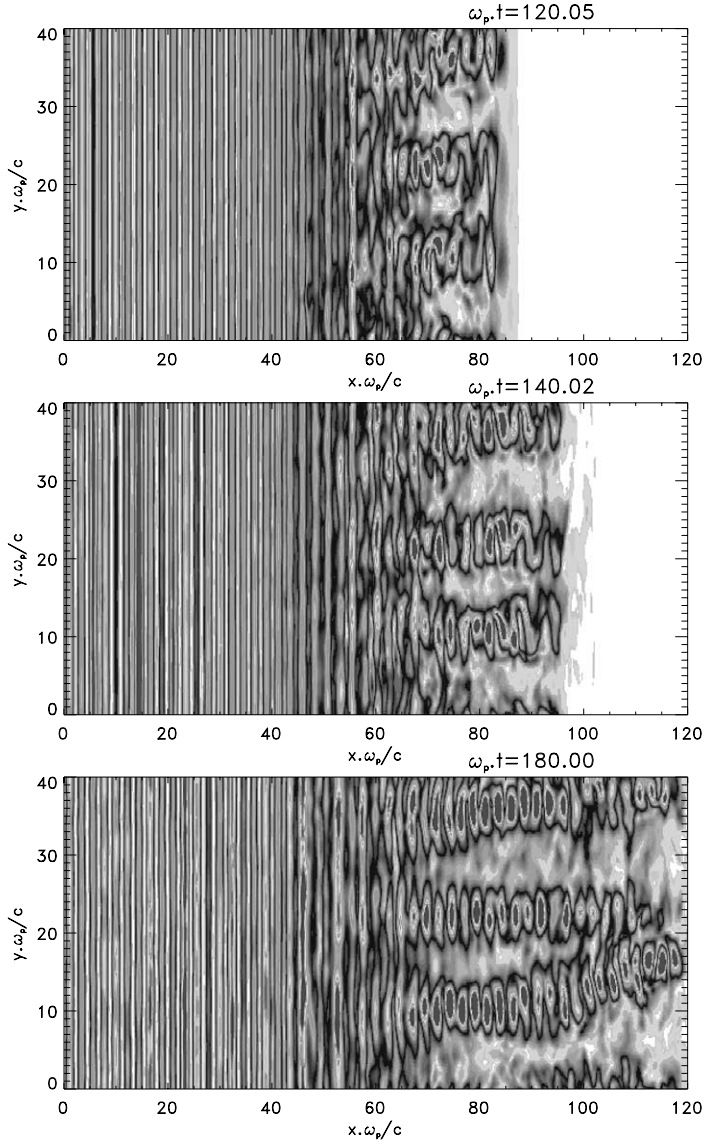

Fig. 12. We have plotted the Poynting vector amplitude plus the relativistic kinetic energy flux at the beginning of RFI using 2D causal SLV simulations: we see clearly the formation of three filaments in the transverse direction. The parameters are $n/n_{\mathrm{crit}} = 0.50$ and $a_0 = \sqrt{3}$.

i.e. the Poynting vector plus the relativistic kinetic energy flux during the time evolution. Another possibility to explore transverse effects is the plot of the (normalized) total energy density (including the relativistic kinetic energy density)

$$w = mc^2 \int\int (\gamma - 1) f \, \mathrm{d}p_x \, \mathrm{d}p_y + \frac{1}{2}\varepsilon_0 E^2 + \frac{B^2}{2\mu_0} \tag{56}$$

Indeed the total energy conservation reads

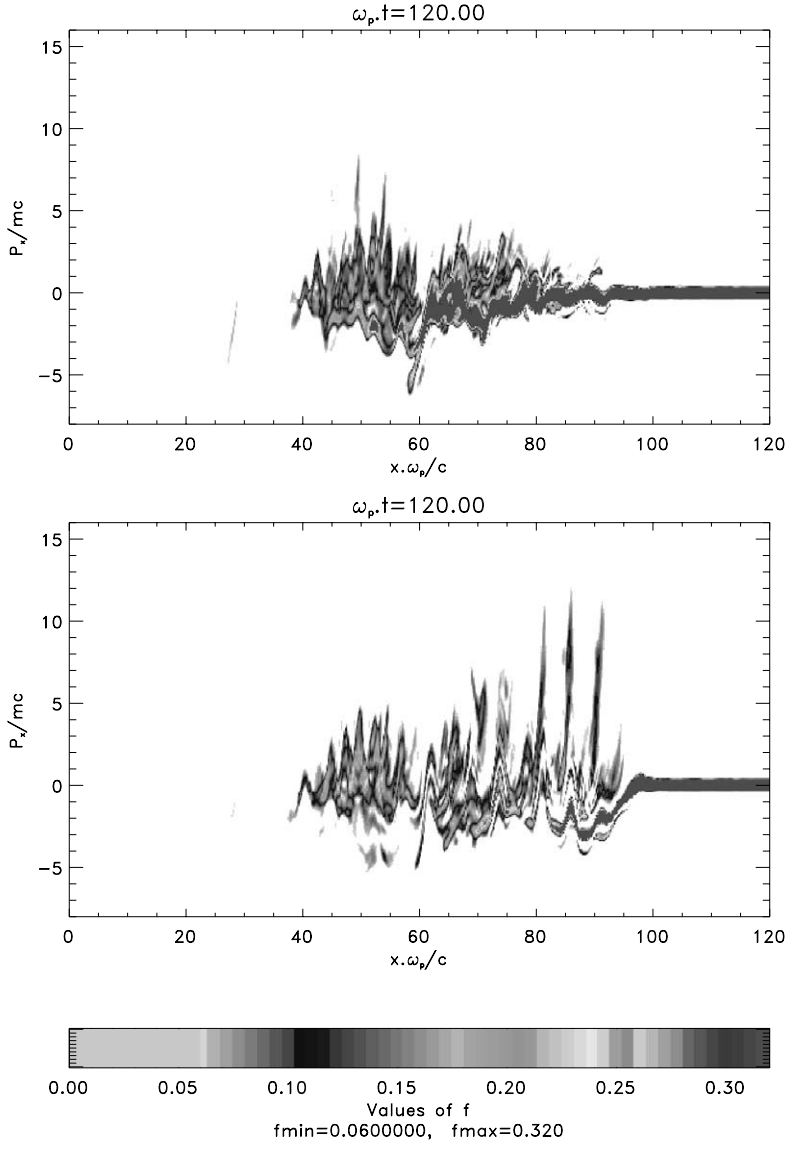

Fig. 13. x–p_x phase space representation of the electron distribution function at time $t\omega_p = 120$. The curves show the particle dynamics outside the filament at $y\omega_p/c = 5$ (above) and inside the filament at $y\omega_p/c = 10$ (below). We see strong acceleration process inside the filament located near the wave front followed by modulation of the plasma bulk induced by RMI.

$$\frac{\partial w}{\partial t} + \nabla.\mathbf{S} = 0. \tag{57}$$

Fig. 12 shows clearly the formation of filaments induced by RFI in the transverse direction of propagation of the laser light with peaks intensity which reach three times the initial values of the initial Poynting vector amplitude $S_0/n_e mc^3 = (eE_0/m\omega_p c)^2 = 6$ (the numerical estimation was $S/n_e mc^3 \simeq 19.4$ at time $t\omega_p = 140$).

Fig. 13 shows the $x - p_x$ electron distribution function at time $t\omega_p = 120$, located outside the filament (at $y\omega_p/c \simeq 5$) and inside the filament for the second curve (located at $y\omega_p/c \simeq 10$). The function has been

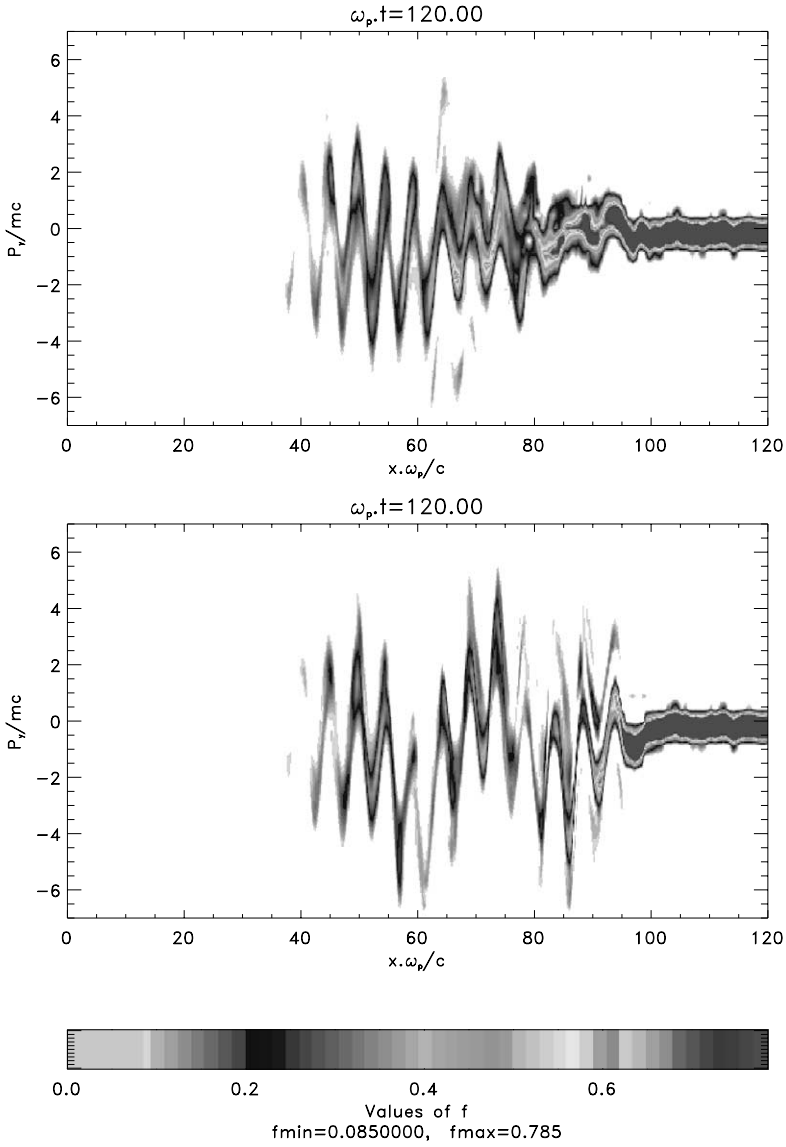

Fig. 14. Corresponding x–p_y phase space representation at the same time as Fig. 13 outside the filament (above) and inside (below): we see inside the filament the occurring of a second modulation on a mode $3k_0$.

averaged over the p_y variable. The bulk of the electron distribution function is strongly affected inside the filament with a particle acceleration mechanism located near the front wave, followed by the modulation of the plasma bulk induced by RMI.

Fig. 14 displays the corresponding x–p_y phase space representation now averaged over the p_x variable. Again the first plot shows the behavior of f outside the filament and the second plot inside the filament. Both curves exhibit the usual modulation induced by the laser pulse corresponding to the relativistic transverse quiver momentum seen by particles. However we see now clearly inside the filament a second modulation on the mode $3k_0$, k_0 being the electromagnetic mode, induced by RMI. These curves show the importance of kinetic effects in the study of the RFI. It is clear that describing the population of trapped particles will require a very detailed analysis of the wave–particle dynamics. However a better understanding of these processes requires a global view of the distribution function in a 4D phase space which is a real challenge.

6. Conclusion

In summary, for the first time a 2D semi-Lagrangian Vlasov scheme in an open system has been assembled to simulate the interaction of an ultra-intense electromagnetic wave with a plasma. Due to the extremely large computational resources required for treating the distribution function described in a four phase space variable, the use of a massively parallel computer was necessary and enabling. A Vlasov algorithm including relativistic effects was developed in a multi-computer environment and implemented on the Cray-T3E computer. This code employs a classic time splitting scheme, cubic spline interpolation or B-Spline interpolation and global synchronous message passing calls using the MPI library for communications between processors. The performance and accuracy obtained in the examples presented here are very satisfying. The SLV code in two dimensions may be a good candidate to explore and understand complex processes induced by the laser–plasma interaction in a strongly relativistic regime and for moderately underdense or overdense plasmas. Finally, obtaining precise insight into the kinetic behavior of the laser–plasma interaction in a 2D system is now possible with semi-Lagrangian Vlasov model, which can provide a great deal of resolution in phase space.

Acknowledgements

We thank J.C. Adam, P. Mora, A. Héron, T.W. Johnston for helpful comments and suggestions. The authors are indebted to the IDRIS Center (Institut du Développement et des Ressources en Informatique Scientifique, Orsay, France) for time allocation on the Cray T3E and NEC SX5 supercomputers.

References

[1] P. Bertrand, A. Ghizzo, T.W. Johnston, M. Shoucri, E. Fijalkow, M.R. Feix, A non periodic Euler–Vlasov code for the numerical simulation of laser–plasma beat wave acceleration and Raman scattering, Phys. Fluids B 2 (5) (1990) 1028.
[2] A. Ghizzo, P. Bertrand, J. Lebas, T.W. Johnston, M. Shoucri, A hybrid Eulerian Vlasov code: I. Study of high frequency beatwave experiment and Manley–Rowe evolution in a finite causal system, Phys. Plasmas 3 (1996) 650.
[3] E. Fijalkow, Behavior of phase space holes in 2D simulations, J. Plasma Phys. 61 (1999) 65.
[4] M.L. Begue, A. Ghizzo, P. Bertrand, E. Sonnendrücker, O. Coulaud, Two-dimensional semi-Lagrangian Vlasov simulations of laser–plasma interaction in the relativistic regime, J. Plasma Phys. 62 (1999) 367.
[5] C.Z. Cheng, G. Knorr, The integration of the Vlasov equation in configuration space, J. Comput. Phys. 22 (1976) 330.
[6] E. Sonnendrücker, J. Roche, P. Bertrand, A. Ghizzo, The semi-Lagrangian method for the numerical resolution of Vlasov equations, J. Comput. Phys. 149 (1999) 201.

[7] R. Bermejo, Analysis of an algorithm for the Galerkin characteristic method, Numer. Math. 60 (1991) 163.
[8] M.L. Begue, A. Ghizzo, P. Bertrand, Two dimensional Vlasov simulations of Raman scattering and plasma beatwave acceleration on parallel computers, J. Comput. Phys. 151 (1999) 458.
[9] A. Staniforth, J. Côte, Semi-Lagrangian integration schemes for atmospheric model. A review, Monthly Weather Rev. 119 (1991) 2206.
[10] O. Coulaud, E. Sonnendrücker, E. Dillon, P. Bertrand, A. Ghizzo, Parallelization of semi-Lagrangian Vlasov codes, J. Plasma Phys. 61 (1999) 435.
[11] A.B. Langdon, On enforcing Gauss' law in electromagnetism particle-in-cell codes, Comput. Phys. Commun. 70 (1992) 447.
[12] J. Villasenor, O. Buneman, Rigorous charge conservation for local electromagnetic field solvers, Comput. Phys. Commun. 69 (1992) 306.
[13] W.H. Press, S.A. Teukolsky, W.T. Vetterling, B.P. Flannery, Numerical Recepies in Fortran, second ed., Cambridge University Press, Cambridge, MA.
[14] O. Buneman, in: O. Buneman, W. Pardo (Eds.), Relativistic Plasma, Benjamin, New York, p. 205.
[15] F. Filbet, E. Sonnendrücker, P. Bertrand, Conservative numerical schemes for the Vlasov equations, J. Comput. Phys. 172 (2001) 166.
[16] A. Mangeney, F. Califano, C. Cavazzoni, P. Travnicek, A numerical scheme for the integration of Vlasov–Maxwell system of equations, J. Comput. Phys. 179 (2002) 495.
[17] F. Huot, A. Ghizzo, P. Bertrand, E. Sonnendrücker, O. Coulaud, Study of propagation of ultra-intense electromagnetic wave through plasma using semi-Lagrangian Vlasov code, IEEE Trans. Plasma Sci. 28 (4) (2000) 1209.